JOURNAL OF THEORETICAL
AND APPLIED MECHANICS
64, 1, pp. 85–97, Warsaw 2026
https://doi.org/10.15632/jtam-pl/217048

MACHINE LEARNING-AUGMENTED UNIVERSAL WEIGHT FUNCTION METHOD FOR STRESS INTENSITY FACTOR DETERMINATION

Kaimin GUO*, Wei TANG, Zijiang YANG, Changxi WANG, Tianyu SUN

China Aero-Polytechnology Establishment, Beijing, China
*corresponding author, *dr_guokaimin@163.com*

The accurate calculation of stress intensity factors (SIFs) constitutes a critical yet challenging task within linear elastic fracture mechanics. While the universal weight function method (WFM) has emerged as a prominent approach due to its high computational efficiency, its predictive accuracy is often constrained. This limitation arises from the difficulty in characterizing the nonlinear mapping relationships between the geometric dimensions of cracked bodies and the requisite weight function parameters. To address these challenges, this study introduces an innovative machine learning-augmented universal WFM. This method leverages Gaussian process regression (GPR) models to characterize the nonlinear mapping relationships between the geometric dimensions of cracked bodies and the weight function parameters, thereby enhancing the computational accuracy of the universal WFM. Validation cases demonstrate that the proposed method achieves superior accuracy compared to the traditional universal WFM, with the maximum relative error not exceeding 5.09 %.

Keywords: stress intensity factor solutions, weight function method, machine learning, Gaussian process regression, a corner crack at a hole.

1. Introduction

Under linear elastic and small-scale yielding conditions, the stress intensity factor (SIF, commonly denoted as K) serves as the fundamental parameter characterizing the crack-tip stress field and the primary driving force for crack propagation. The accuracy of SIF calculations directly governs the reliability of crack growth life predictions, rendering its computational methodology a central focus in linear elastic fracture mechanics research.

Closed-form solutions, finite element methods (FEMs), weight function methods (WFMs), and machine learning-based approaches represent principal computational methodologies for determining SIFs (McClung *et al.*, 2013). Closed-form equations were proposed in (Newman & Raju, 1981; 1984; Raju & Newman, 1979). Their fundamental principle resides in fitting SIFs, obtained from extensive FEM calculations, into explicit closed-form equations. During computation, one simply substitutes the geometric and characteristic parameters into these closed-form equations. This approach is computationally efficient, requiring minimal computational effort. However, its applicability is restricted to simple geometric configurations and basic loading conditions, specifically remote tension and bending. Commercial finite element analysis (FEA) software packages offer high computational accuracy and represent an effective tool for determining SIFs (Wawrzynek *et al.*, 2010; Xiao & Yan, 2008). However, it should be noted that while the FEM inherently provides high accuracy, it inevitably suffers from computational inefficiency. For complex geometries, crack configurations, and loading conditions, FEM analyses typically entail substantial computational time and significant computational expenses. Propelled by rapid advances in artificial intelligence and data-driven technologies, machine learning (ML) has emerged

as a prominent research focus for predicting SIFs (Guo *et al.*, 2024; Keprate *et al.*, 2017; Muñoz-Abella *et al.*, 2015). The principal advantage of ML methodologies lies in their computational efficiency and expediency: once an ML model is adequately trained, SIF values for arbitrary loading conditions and structural configurations can be rapidly obtained.

The WFM represents a mainstream computational approach for determining SIFs, offering a balanced compromise between computational accuracy and efficiency (Chen & Wang, 2004; Evans *et al.*, 2014; Glinka & Shen, 1991; Shen & Glinka, 1991a; Vainshtok & Varfolomeyev, 1990; Zheng *et al.*, 1996). Its fundamental principle lies in decoupling the two primary factors influencing SIF calculations – geometry and loading. Specifically, the SIF is expressed as the integral of the product of the weight function and the applied loading distribution along the crack length (Yang *et al.*, 2013).

A complex nonlinear relationship exists between the key parameters within the weight function and the crack geometry dimensions. In the conventional derivation of universal weight functions, polynomial fitting methods are commonly employed to describe this nonlinear relationship. However, the resulting fitting coefficients, often exceeding one hundred terms, impose a significant computational burden and hinder the practical application of the WFM (Ghajar & Saeidi Googarchin, 2013; Shen & Glinka, 1991b; Shen *et al.*, 1991; Wang & Lambert, 1995a; 1995b; Yang *et al.*, 2013). Due to the inability to accurately characterize the nonlinear relationship between the key parameters and the geometric dimensions, the universal WFM exhibits inherent limitations in predictive accuracy. Consequently, the adoption of advanced fitting techniques is necessitated to precisely capture the nonlinear relationship between the key parameters and the crack body geometry, thereby enhancing the computational accuracy of the universal WFM.

This study proposes an innovative machine learning-augmented universal WFM designed to characterize the nonlinear mapping between cracked body geometry dimensions and weight function parameters, thereby enhancing the computational accuracy of SIFs. Initially, the fundamental principles and derivation process of the universal weight function are demonstrated using a corner crack at a hole as a representative case study. Subsequently, the proposed ML-augmented WFM is presented, whose core involves employing a Gaussian process regression (GPR) model to characterize the nonlinear mapping relationships between the geometric dimensions of the cracked body and the weight function parameters. Finally, the predictive accuracy of the proposed method is demonstrated through the calculation of the SIF for the corner crack at a hole under new loading conditions.

2. Derivation procedure of the universal WFM

In this section, a corner crack at a hole is employed as a case study to elucidate the physical significance of the crack body's geometric dimensions. Subsequently, this corner crack at a hole is used as an example to demonstrate the derivation procedure of the universal WFM.

2.1. A corner crack at a hole

Taking an aero-engine turbine disk as an example, it contains various functional holes – such as the central bore hole, dowel holes, and eccentric holes – which are prone to crack initiation and propagation. A simplified model of the corner crack at one such hole is illustrated in Fig. 1.

A plate of thickness t contains a central hole of radius r. A quarter-elliptical corner crack emanates from one side of the hole, with its depth direction aligned with the plate thickness direction. The crack surface experiences uniaxial stress variation; under non-uniformly distributed stress, the stress varies solely along the y-axis (i.e., the plate thickness direction). In the schematic, a denotes the crack depth, and c represents the surface crack length. Point A, the deepest vertex of the crack front located at the hole surface, is hereafter termed the "hole-surface point". Point B, the surface vertex on the plate face, is designated as the "plate-surface point".

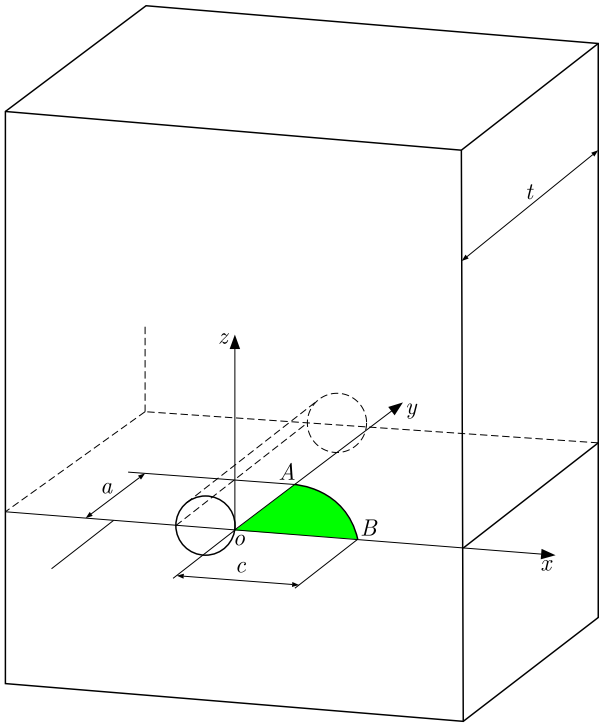

Fig. 1. Corner crack at a hole.

2.2. Stress intensity factor data acquisition

The principle of the universal WFM states that the SIF is calculated as the integral of the product of the weight function and the nominal stress along the crack length, as expressed in Eq. (2.1). Here, $m(y,a)$ denotes the weight function – a parameter independent of loading conditions and solely dependent on geometric configuration and crack morphology. The variable a represents crack length, while $\sigma(y)$ signifies the stress acting on the crack face, specifically defined as the nominal stress on the prospective crack plane in the imaginary uncracked structure. Within weight function theory, once the weight function $m(y,a)$ for a given crack type is determined, the SIF under any arbitrary loading can be computed using Eq. (2.1):

$$K = \int_0^a \sigma(y) m(y,a)\,\mathrm{d}y. \tag{2.1}$$

The derivation procedure for the universal weight function pertaining to corner cracks emanating from a hole entails several key steps. Firstly, a comprehensive dataset of SIFs for the corner crack, corresponding to various geometric configurations, is compiled utilizing numerical methods such as the FEM. This dataset serves as the foundational input. Subsequently, reference SIFs are derived through curve fitting techniques. Finally, these fitted reference SIFs are substituted into the governing weight function equation (Eq. (2.1)) to inversely solve it for the universal weight function itself. Each step is elaborated in Subsection 2.2 to 2.4.

In this study, the FEM is employed to compute the reference SIFs for corner cracks at a hole. The key geometric parameters characterizing the configuration, comprising a circular hole and associated corner cracks, include the crack dimensions a and c, the plate thickness t, and the hole radius r. The SIF data for corner cracks emanating from a hole, computed via FEA, serve as input data for subsequent fitting of reference SIFs.

To ensure the derived weight function provides comprehensive coverage over a broad range of crack sizes, the reference solutions encompass the following dimensional ranges: $0.2 \leq a/c \leq 1$, $0.2 \leq a/t \leq 0.8$ and $0.3 \leq r/t \leq 2$. To span this domain, 100 distinct configurations were

analyzed, combining the parameters $r/t = \{0.3, 0.5, 1, 1.5, 2\}$, $a/t = \{0.2, 0.4, 0.6, 0.8\}$ and $a/c = \{0.2, 0.4, 0.6, 0.8, 1\}$. Additionally, the plate dimensions were specified as thickness $t = 10\,\text{mm}$, width $W = 50\,\text{mm}$, and the semi-height of the cracked plate is 100 mm.

The universal weight function methodology requires that the two reference loading cases exhibit distinct polynomial orders along the same coordinate axis. Considering load distributions along the y-axis as an illustrative case, the functional forms of these reference loads must incorporate different exponents of y. Consistent with this selection principle, a uniformly distributed load and a linearly distributed load were selected as reference cases. Their mathematical expressions and schematic representations are provided in Eq. (2.2) and Fig. 2, respectively, where $\sigma_0 = 200\,\text{MPa}$:

$$\begin{aligned} \sigma_{r1}(y) &= \sigma_0, \\ \sigma_{r2}(y) &= \sigma_0 \left(1 - \frac{y}{a}\right). \end{aligned} \tag{2.2}$$

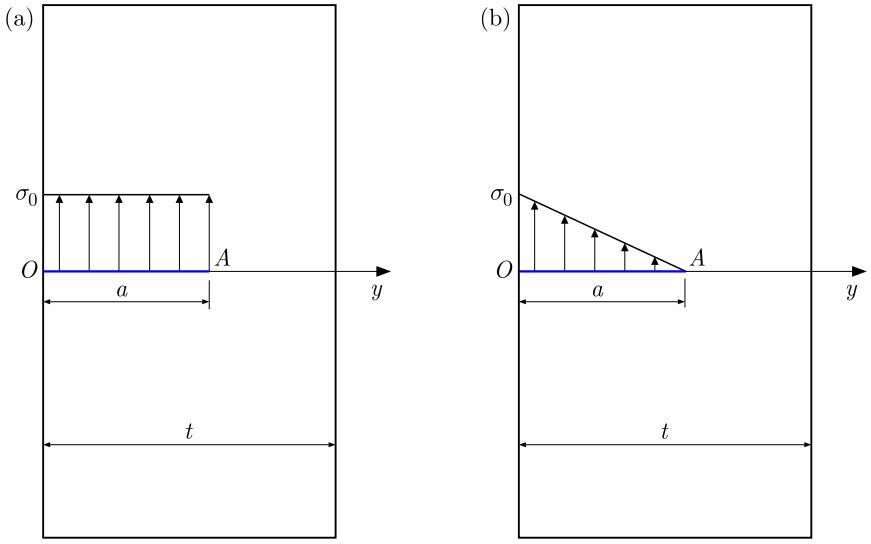

Fig. 2. Two reference loading cases: (a) a uniformly distributed load and (b) a linearly distributed load.

For a corner crack at a hole, 200 sets of SIF data were computed via the aforementioned FEM under uniformly distributed and linearly distributed loads. Selected partial computed SIF results are presented in Table 1.

Table 1. Partial computed SIF results for the corner crack at a hole (unit: $\text{MPa} \cdot \text{m}^{1/2}$).

Geometric dimensions [mm]				Uniformly distributed load		Linearly distributed load	
t	r	a	c	Point A	Point B	Point A	Point B
10	3	2	2	**9.87**	**10.47**	**2.69**	**8.98**
	5	4	10	**18.8**	**16.21**	**6.61**	**13.59**
	10	6	15	**26.64**	**23.84**	**10.26**	**19.41**
	15	8	40	**47.62**	**40.81**	**21.68**	**31.68**
	20	2	2.5	**11.73**	**11.11**	**3.61**	**9.4**

2.3. Weight functions for the hole-surface point (point *A*)

The fitted reference SIFs at point A are given by Eqs. (2.3) and (2.4), corresponding to the uniformly distributed load and linearly distributed load cases, respectively:

$$K_{r1}^{A} = \sigma_0 \sqrt{\frac{\pi a}{Q}} F_0^A, \tag{2.3}$$

$$K_{r2}^{A} = \sigma_0 \sqrt{\frac{\pi a}{Q}} F_1^A, \tag{2.4}$$

where Q denotes an elliptical integral of the second kind as follows:

$$\begin{aligned} Q &= 1 + 1.464 \left(\frac{a}{c}\right)^{1.65} && \text{for} \quad \frac{a}{c} \le 1, \\ Q &= \left[1 + 1.464 \left(\frac{c}{a}\right)^{1.65}\right] \left(\frac{a}{c}\right)^{2} && \text{for} \quad \frac{a}{c} > 1. \end{aligned} \tag{2.5}$$

The geometric correction factors F_0^A and F_1^A in Eqs. (2.3) and (2.4) are defined by Eqs. (2.6) and (2.7), respectively, with their fitting coefficients (F_{ijk}^{A0} and F_{ijk}^{A1}) provided in Table 2 and Table 3:

$$F_0^A = \sum_{i=0}^{4} \sum_{j=0}^{4} \sum_{k=0}^{4} F_{ijk}^{A0} \left(\frac{r}{t}\right)^i \left(\frac{a}{t}\right)^j \left(\frac{a}{c}\right)^k \qquad (i + j + k \le 4), \tag{2.6}$$

$$F_1^A = \sum_{i=0}^{4} \sum_{j=0}^{4} \sum_{k=0}^{4} F_{ijk}^{A1} \left(\frac{r}{t}\right)^i \left(\frac{a}{t}\right)^j \left(\frac{a}{c}\right)^k \qquad (i + j + k \le 4). \tag{2.7}$$

Table 2. Fitting coefficients F_{ijk}^{A0}.

ijk	**000**	**100**	**010**	**001**	**200**	**110**	**020**	**101**
F_{ijk}^{A0}	0.80987	0.43996	0.31255	−0.33554	−0.53319	0.89868	1.0763	−0.32291
ijk	**011**	**002**	**300**	**210**	**120**	**030**	**201**	**111**
F_{ijk}^{A0}	−3.8205	2.3282	0.28616	−0.39388	0.42119	0	0.099301	−1.0692
ijk	**021**	**102**	**012**	**003**	**400**	**310**	**220**	**130**
F_{ijk}^{A0}	−2.1016	0.67762	6.1776	−3.6767	−0.054743	0.050831	0.058895	0.067399
ijk	**040**	**301**	**211**	**121**	**031**	**202**	**112**	**022**
F_{ijk}^{A0}	−1.5952	−0.010479	0.082393	−0.68089	3.4542	−0.062899	0.93604	−1.2303
ijk	**103**	**013**	**004**					
F_{ijk}^{A0}	−0.43519	−2.5408	1.7877					

Table 3. Fitting coefficients F_{ijk}^{A1}.

ijk	**000**	**100**	**010**	**001**	**200**	**110**	**020**	**101**
F_{ijk}^{A1}	0.26186	0.20553	0.25101	−0.20993	−0.23079	0.39053	0.81609	−0.21552
ijk	**011**	**002**	**300**	**210**	**120**	**030**	**201**	**111**
F_{ijk}^{A1}	−2.2418	1.2155	0.12163	−0.19866	0.4733	0	0.077674	−0.76695
ijk	**021**	**102**	**012**	**003**	**400**	**310**	**220**	**130**
F_{ijk}^{A1}	−1.7481	0.45305	3.9868	−2.1541	−0.022975	0.026659	0.010877	−0.020452
ijk	**040**	**301**	**211**	**121**	**031**	**202**	**112**	**022**
F_{ijk}^{A1}	−1.2667	−0.011164	0.068314	−0.4424	2.4765	−0.042608	0.62347	−0.7467
ijk	**103**	**013**	**004**					
F_{ijk}^{A1}	−0.29034	−1.6712	1.0968					

The key parameters (M_{1A}, M_{2A}, and M_{3A}) of the weight function at point A were determined by substituting the fitted reference SIFs into the weight function integration procedure and solving the inverse problem.

In (Zheng *et al.*, 1996), the weight function of point A is calculated as Eq. (2.8), and the corresponding weight function is expressed as Eq. (2.9):

$$K^A = \int_0^a \sigma(y) m_A(y,a)\,\mathrm{d}y, \tag{2.8}$$

$$m_A(y,a) = \frac{2}{\sqrt{2\pi(a-y)}}\left[1 + M_{1A}\left(1-\frac{y}{a}\right)^{1/2} + M_{2A}\left(1-\frac{y}{a}\right) + M_{3A}\left(1-\frac{y}{a}\right)^{3/2}\right]. \tag{2.9}$$

Synthesis of the aforementioned procedures with the solution methodology described in (Zheng *et al.*, 1996) yields the three key parameters (M_{1A}, M_{2A}, and M_{3A}) of the weight function at point A, as expressed in Eq (2.10):

$$\begin{aligned} M_{1A} &= \frac{\pi}{\sqrt{2Q}}(4F_0^A - 6F_1^A) - \frac{24}{5}, \\ M_{2A} &= 3, \\ M_{3A} &= 2\left(\frac{\pi}{\sqrt{2Q}}F_0^A - M_{1A} - 4\right). \end{aligned} \tag{2.10}$$

2.4. Weight functions for the plate-surface point (point B)

Similarly, the fitted reference SIFs at point B are given by Eqs. (2.11) and (2.12), corresponding to the uniformly distributed load and linearly distributed load cases, respectively:

$$K_{r1}^B = \sigma_0\sqrt{\frac{\pi a}{Q}}F_0^B, \tag{2.11}$$

$$K_{r2}^B = \sigma_0\sqrt{\frac{\pi a}{Q}}F_1^B, \tag{2.12}$$

where Q likewise represents an elliptic integral of the second kind, as given in Eq. (2.5).

The geometric correction factors F_0^B and F_1^B in Eqs. (2.11) and (2.12) are defined by Eqs. (2.13) and (2.14), respectively, with their fitting coefficients (F_{ijk}^{B0} and F_{ijk}^{B1}) provided in Table 4 and Table 5:

$$F_0^B = \sum_{i=0}^{4}\sum_{j=0}^{4}\sum_{k=0}^{4} F_{ijk}^{B0}\left(\frac{r}{t}\right)^i\left(\frac{a}{t}\right)^j\left(\frac{a}{c}\right)^k \qquad (i+j+k\le 4), \tag{2.13}$$

$$F_1^B = \sum_{i=0}^{4}\sum_{j=0}^{4}\sum_{k=0}^{4} F_{ijk}^{B1}\left(\frac{r}{t}\right)^i\left(\frac{a}{t}\right)^j\left(\frac{a}{c}\right)^k \qquad (i+j+k\le 4). \tag{2.14}$$

In (Zheng *et al.*, 1996), the weight function of point B is calculated as Eq. (2.15), and the corresponding weight function is expressed as Eq. (2.16):

$$K^B = \int_0^a \sigma(y) m_B(y,a)\,\mathrm{d}y, \tag{2.15}$$

$$m_B(y,a) = \frac{2}{\sqrt{\pi y}}\left[1 + M_{1B}\left(\frac{y}{a}\right)^{1/2} + M_{2B}\left(\frac{y}{a}\right) + M_{3B}\left(\frac{y}{a}\right)^{3/2}\right]. \tag{2.16}$$

Table 4. Fitting coefficients F_{ijk}^{B0}.

ijk	**000**	**100**	**010**	**001**	**200**	**110**	**020**	**101**
F_{ijk}^{B0}	0.18934	0.001833	−0.21587	2.2489	−0.035908	0.05961	1.2912	0.14708
ijk	**011**	**002**	**300**	**210**	**120**	**030**	**201**	**111**
F_{ijk}^{B0}	0.22558	−2.9939	0.033293	−0.12234	0.40337	0	−0.077422	0.018976
ijk	**021**	**102**	**012**	**003**	**400**	**310**	**220**	**130**
F_{ijk}^{B0}	−3.0223	−0.017841	1.5578	1.7403	−0.0080764	0.026938	−0.029182	0.057118
ijk	**040**	**301**	**211**	**121**	**031**	**202**	**112**	**022**
F_{ijk}^{B0}	0.92792	0.016252	−0.00075897	−0.33759	−3.0408	0.0049268	0.15513	5.0755
ijk	**103**	**013**	**004**					
F_{ijk}^{B0}	−0.032284	−2.8907	−0.018604					

Table 5. Fitting coefficients F_{ijk}^{B1}.

ijk	**000**	**100**	**010**	**001**	**200**	**110**	**020**	**101**
F_{ijk}^{B1}	0.19763	−0.00029338	−0.13599	1.8091	−0.020001	0.033383	0.87295	0.099138
ijk	**011**	**002**	**300**	**210**	**120**	**030**	**201**	**111**
F_{ijk}^{B1}	0.096081	−2.4811	0.018856	−0.076752	0.26425	0	−0.054186	0.019809
ijk	**021**	**102**	**012**	**003**	**400**	**310**	**220**	**130**
F_{ijk}^{B1}	−2.0522	−0.010023	1.1515	1.6063	−0.0046192	0.017855	−0.023746	0.05524
ijk	**040**	**301**	**211**	**121**	**031**	**202**	**112**	**022**
F_{ijk}^{B1}	0.70579	0.012017	−0.0030259	−0.23092	−2.1742	0.0018728	0.10586	3.5405
ijk	**103**	**013**	**004**					
F_{ijk}^{B1}	−0.02068	−2.0474	−0.15014					

Synthesis of the aforementioned procedures with the solution methodology described in (Zheng *et al.*, 1996) yields the three key parameters (M_{1B}, M_{2B}, and M_{3B}) of the weight function at point B, as expressed in Eq. (2.17):

$$\begin{aligned} M_{1B} &= \frac{\pi}{\sqrt{4Q}}(30F_1^B - 18F_0^B) - 8, \\ M_{2B} &= \frac{\pi}{\sqrt{4Q}}(60F_0^B - 90F_1^B) + 15, \\ M_{3B} &= -(1 + M_{1B} + M_{2B}). \end{aligned} \tag{2.17}$$

3. ML-augmented WFM

From the derivation process of the aforementioned universal WFM, it can be concluded that establishing an accurate mapping relationship between the geometric correction factors of reference SIFs and the geometric dimensions of the cracked body is crucial for developing the universal WFM. For the aforementioned corner crack at a hole, the mapping relationship between the geometric correction factors of reference SIFs and the geometric dimensions of the cracked body is given by

$$F = f\left(\frac{r}{t}, \frac{a}{t}, \frac{a}{c}\right), \tag{3.1}$$

where F is the geometric correction factor, characterizing the influence of the cracked body's geometric dimensions on the SIF, and a/c, a/t, and r/t represent the geometric dimensions

of the corner crack at a hole. A complex nonlinear mapping relationship exists between the geometric correction factor (F) and these geometric dimensions (a/c, a/t, and r/t). In previous studies, polynomial fitting and similar means were typically utilized to establish this mapping relationship.

In this study, the nonlinear mapping relationship within the aforementioned universal WFM is developed using a GPR model.

3.1. Process for establishing mapping relationships using GPR

The GPR model, also known as the Kriging model, is an interpolation method based on Gaussian processes governed by a priori covariance (Rasmussen, 2004; Rasmussen & Williams, 2005). It provides both the mean and standard deviation as outputs during prediction, thereby offering a probabilistic prediction framework. As a non-parametric model, it falls under the umbrella of supervised learning.

The GPR algorithm can be mathematically formulated as Eq. (3.2), where $m(x)$ and $k(x,x')$ denote the mean function and covariance function, respectively. This formulation signifies that the function f follows a Gaussian distribution characterized by the mean function m and covariance kernel k:

$$f \sim \mathrm{GP}(m(x), k(x, x')). \tag{3.2}$$

The GPR model was employed to approximate the nonlinear relationships. This approximation procedure is also referred to as training the GPR model. During model training, an iterative optimization scheme was implemented with the objective of minimizing the mean squared error (MSE), as illustrated in Fig. 3. The minimum MSE was achieved after 25 iterations, indicating the completion of the model training process. On the workstation (Processor: i5-13600KF (3.50 GHz), RAM: 32.0 GB), the time required for the aforementioned training process is 9.3385 seconds. Once the model is trained, its prediction speed approaches 18 000 observations per second.

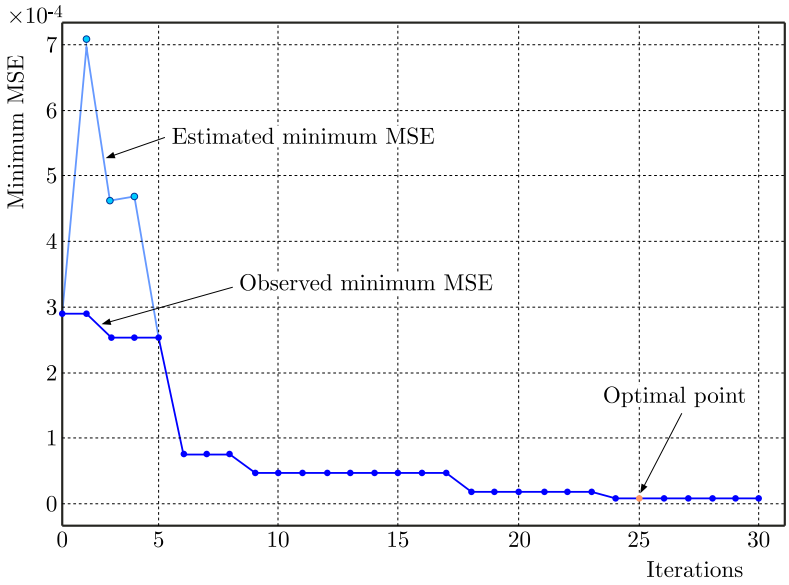

Fig. 3. Iterative training process for GPR model.

To demonstrate the effectiveness of the selected GPR model, a comparison of the prediction accuracy among various ML models was conducted. Specifically, different ML models, as shown in Table 6, were trained using the same training data, and their root mean square error (RMSE) values of the prediction results were compared, as illustrated in Fig. 4. It can be observed that the selected GPR model exhibits a smaller prediction RMSE and higher prediction accuracy.

Table 6. Details of the ML model.

ML model	Parameters of the ML model
Gaussian process regression (GPR)	Basis function: linear, $\sigma = 0.1019$
Support vector regression (SVR)	SVR with a cubic kernel
Artificial neural network (ANN)	Two-layer neural network, number of fully connected layers: 2, activation function: ReLU
Stepwise regression model (SRM)	Maximum number of steps: 1000
Regression tree (RT)	Coarse-grained tree, minimum leaf size: 36

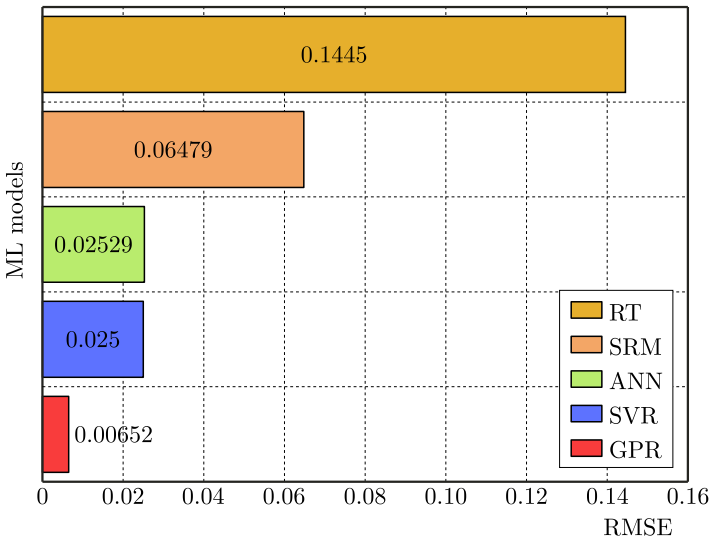

Fig. 4. Comparison of predictive accuracy among different ML models.

3.2. Nonlinear mapping relationship fitting results

The geometric correction factors at point A under the two types of reference loads are denoted as F_0^A and F_1^A. Nonlinear mapping relationships between these geometric correction factors and the geometric dimensions of the crack body were established using GPR models, as given in Eqs. (3.3) and (3.4). Since the fitted results of the GPR models cannot be represented by explicit analytical expressions, Eqs. (3.3) and (3.4) merely serve as representations of the relationships between the input variables and the output variables:

$$F_0^A = f_{0\,\mathrm{GPR}}^A\left(\frac{r}{t}, \frac{a}{t}, \frac{a}{c}\right), \tag{3.3}$$

$$F_1^A = f_{1\,\mathrm{GPR}}^A\left(\frac{r}{t}, \frac{a}{t}, \frac{a}{c}\right). \tag{3.4}$$

Concurrently, nonlinear mapping relationships between the geometric correction factors at point B (F_0^B and F_1^B) and the geometric dimensions of the crack body were established using GPR models, as represented by:

$$F_0^B = f_{0\,\mathrm{GPR}}^B\left(\frac{r}{t}, \frac{a}{t}, \frac{a}{c}\right), \tag{3.5}$$

$$F_1^B = f_{1\,\mathrm{GPR}}^B\left(\frac{r}{t}, \frac{a}{t}, \frac{a}{c}\right). \tag{3.6}$$

SHapley Additive exPlanations (SHAP) values quantify the contribution of each feature to the model output, and are thus widely employed in the field of ML to elucidate the relationship

between inputs and outputs. Figure 5 illustrates the SHAP values of different features (a/c, a/t, and r/t) with respect to the output of the GPR model. In the figure, a larger data width indicates a greater influence of the corresponding feature on the GPR model output. It can be observed that all three features exhibit a strong contribution to the output values.

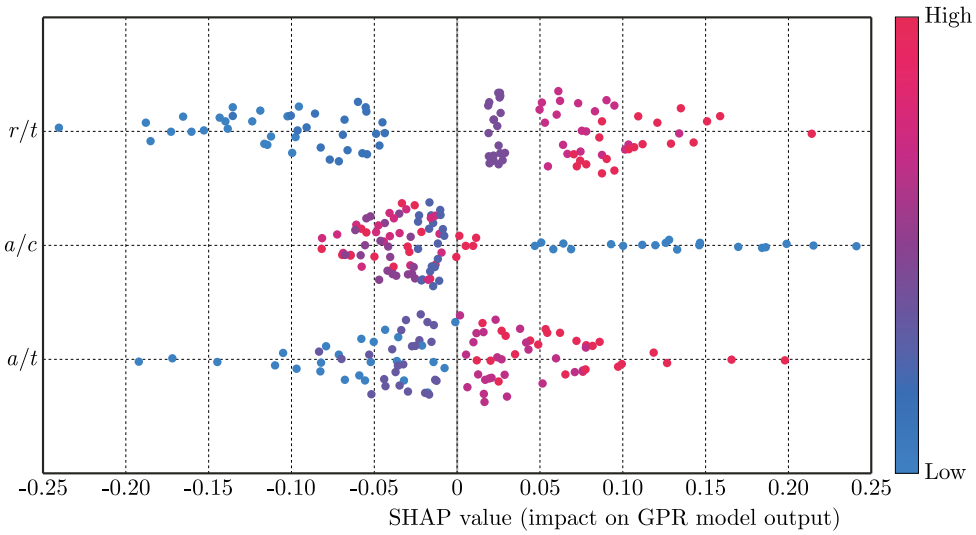

Fig. 5. SHAP values of different features to the GPR model output.

The GPR model predictions of the geometric correction factors at points A and B are presented in Fig. 6. The reference values shown in the figures correspond to the geometric correction

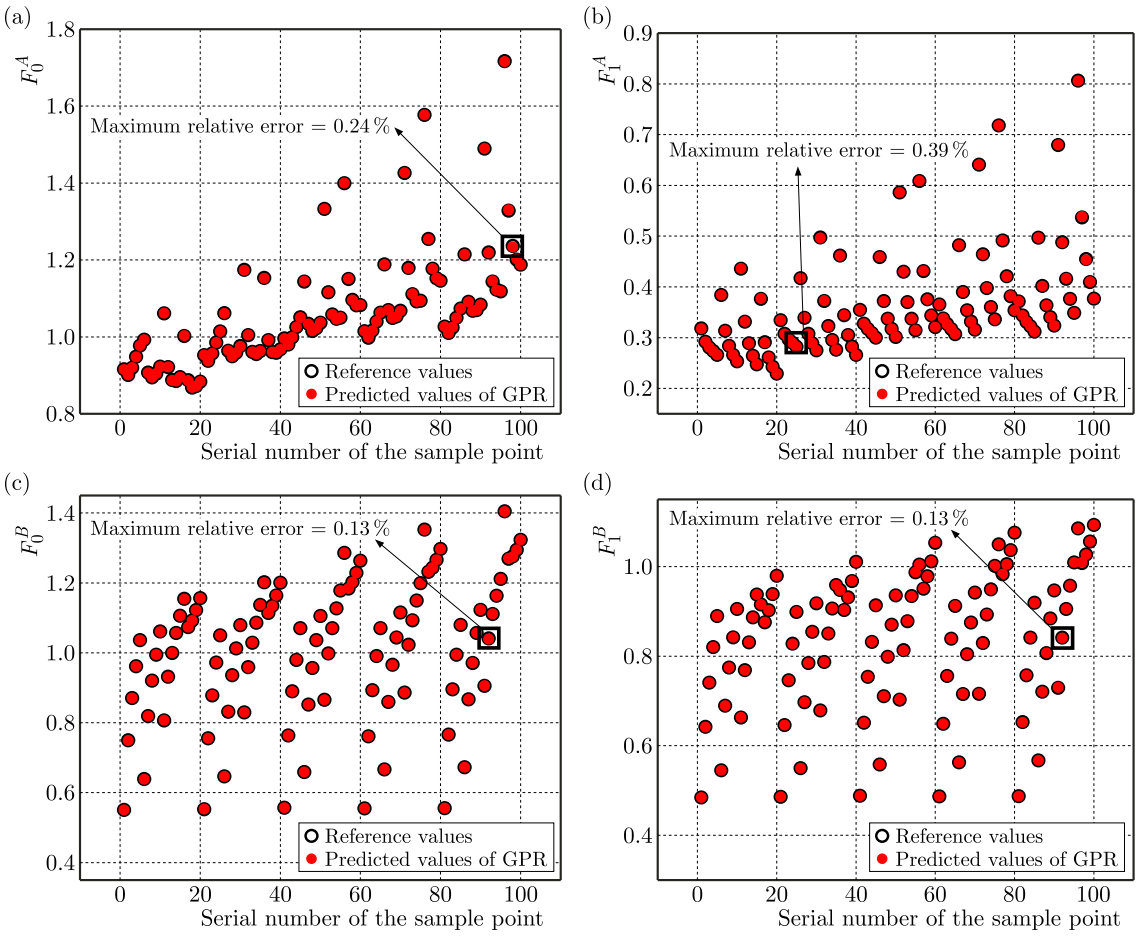

Fig. 6. GPR model prediction results for geometric correction factors: (a) F_0^A; (b) F_1^A; (c) F_0^B; (d) F_1^B.

factors calculated using finite element results for the SIFs. It can be observed that the GPR model, which fits the mapping relationship between the geometric correction factors and the crack body's geometric dimensions, achieves high prediction accuracy, with a maximum relative prediction error of 0.39 %. Upon completing the description of the nonlinear mapping relationships for the universal WFM, these mappings, combined with the universal weight function derived in Section 2, constitute the machine learning-augmented universal WFM.

4. Validation

This section assesses the computational accuracy of the proposed ML-augmented WFM. First, the SIFs for a corner crack at a hole under new stress distribution are computed using: (a) the FEM, (b) the conventional WFM detailed in Section 2, and (c) the proposed ML-augmented WFM. Subsequently, using the FEM results as the benchmark, the prediction accuracy of the other two methods (the conventional WFM and ML-augmented WFM) is compared. The stress distribution applied to the crack in this validation case is given by

$$\sigma(y) = \sigma_0 \left(1 - \frac{y}{a}\right)^n, \qquad n = 2, 3. \tag{4.1}$$

The computed SIFs are presented in Fig. 7 and Fig. 8. It can be observed that the proposed ML-augmented WFM demonstrates enhanced predictive accuracy over the conventional WFM.

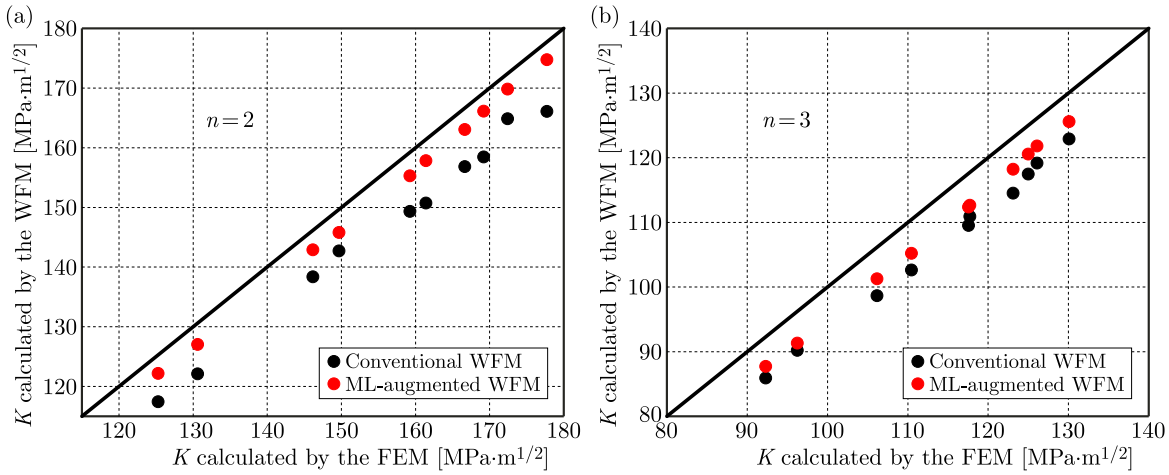

Fig. 7. Computed SIFs at point A: (a) $n = 2$; (b) $n = 3$.

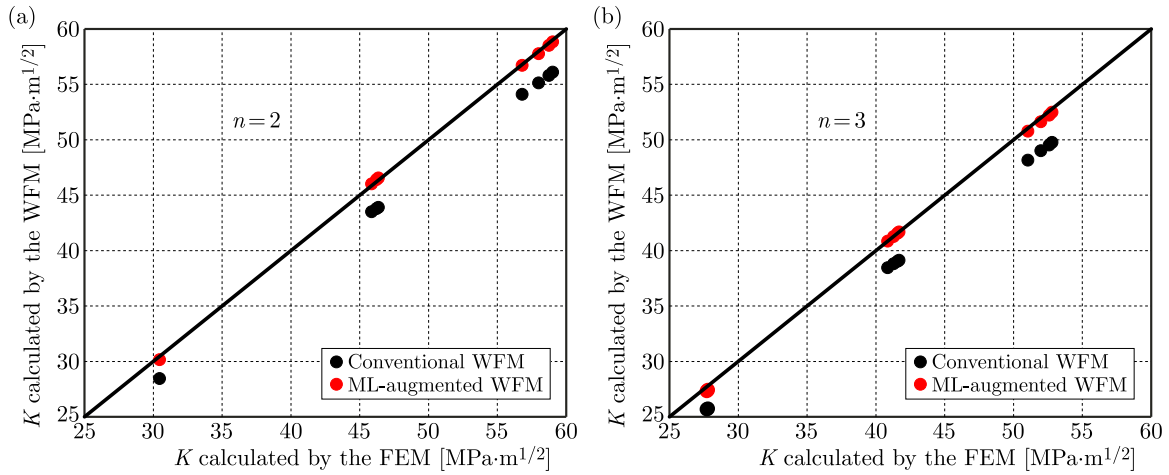

Fig. 8. Computed SIFs at point B: (a) $n = 2$; (b) $n = 3$.

Compared with the FEM results, the maximum relative error of the proposed method is merely 5.09 %.

5. Conclusion

Based on this study, three conclusions are drawn:

1) intricate nonlinear mapping relationships exist between the key parameters in the weight function and the crack geometric dimensions. The predictive accuracy of the universal WFM is limited by its inability to precisely characterize these nonlinear relationships. Therefore, advanced regression techniques are required to accurately describe the nonlinear relationships between the key parameters and the crack body's geometric dimensions, thereby enhancing the computational accuracy of the universal WFM;
2) an innovative machine learning-augmented WFM is proposed to improve the predictive accuracy of the universal WFM. This approach utilizes GPR models to fit the nonlinear mapping relationships between the key parameters in the weight function and the crack geometric dimensions;
3) validation cases demonstrate that the proposed machine learning-augmented WFM outperforms the conventional WFM in terms of predictive accuracy, with the maximum prediction error not exceeding 5.09 %.

Acknowledgments

This study was supported by the National Major Science and Technology Project (grant no. J2019-IV-0007-0075).

References

1. Chen, Q., & Wang, X. (2004). Weight functions and stress intensity factors for quarter-elliptical corner cracks in fastener holes. *Fatigue & Fracture of Engineering Materials and Structures*, *27*(8), 701–712. https://doi.org/10.1111/j.1460-2695.2004.00796.x

2. Evans, R., Clarke, A., Heller, M., & Stewart, R. (2014). Improved stress intensity factors for a single corner crack at a loaded fastener hole. *Engineering Fracture Mechanics*, *131*, 570–586. https://doi.org/10.1016/j.engfracmech.2014.09.012

3. Ghajar, R., & Saeidi Googarchin, H. (2013). General point load weight function for semi-elliptical crack in finite thickness plates. *Engineering Fracture Mechanics*, *109*, 33–44. https://doi.org/10.1016/j.engfracmech.2013.06.007

4. Glinka, G., & Shen, G. (1991). Universal features of weight functions for cracks in mode I. *Engineering Fracture Mechanics*, *40*(6), 1135–1146. https://doi.org/10.1016/0013-7944(91)90177-3

5. Guo, K., Liu, H., Yan, H., Song, Z., Zhang, S., Huang, D., & Yan, X. (2024). Estimation of stress intensity factor for surface cracks in the firtree groove structure of a turbine disk using pool-based active learning with Gaussian Process Regression. *Journal of Theoretical and Applied Mechanics*, *62*(1), 89–101. https://doi.org/10.15632/jtam-pl/174709

6. Keprate, A., Ratnayake, R.M.C., & Sankararaman, S. (2017). Comparison of various surrogate models to predict stress intensity factor of a crack propagating in offshore piping. *Journal of Offshore Mechanics and Arctic Engineering*, *139*(6), Article 061401. https://doi.org/10.1115/1.4037290

7. McClung, R.C., Lee, Y.-D., Cardinal, J.W., & Guo, Y. (2013). The pursuit of K: Reflections on the current state-of-the-art in stress intensity factor solutions for practical aerospace applications. In A. Brot (Ed.), *Proceedings of the 27th Symposium of the International Committee on Aeronautical Fatigue and Structural Integrity: Vol. 1* (pp. 361–375). Israel Society of Aeronautics and Astronautics.

8. Muñoz-Abella, B., Rubio, L., & Rubio, P. (2015). Stress intensity factor estimation for unbalanced rotating cracked shafts by artificial neural networks. *Fatigue & Fracture of Engineering Materials & Structures*, *38*(3), 352–367. https://doi.org/10.1111/ffe.12237

9. Newman Jr, J.C., & Raju, I.S. (1981). *Stress-intensity factor equations for cracks in three-dimensional finite bodies* (NASA Technical Memorandum 83200). National Aeronautics and Space Administration. https://ntrs.nasa.gov/api/citations/19810023035/downloads/19810023035.pdf

10. Newman Jr, J.C., & Raju, I.S. (1984). *Stress-intensity factor equations for cracks in three-dimensional finite bodies subjected to tension and bending loads* (NASA Technical Memorandum 85793). National Aeronautics and Space Administration. https://ntrs.nasa.gov/api/citations/19840015857/downloads/19840015857.pdf

11. Raju, I.S., & Newman Jr, J.C. (1979). Stress-intensity factors for a wide range of semi-elliptical surface cracks in finite-thickness plates. *Engineering Fracture Mechanics*, *11*(4), 817–829. https://doi.org/10.1016/0013-7944(79)90139-5

12. Rasmussen, C.E. (2004). Gaussian processes in machine learning. In O. Bousquet, U. von Luxburg, & G. Rätsch (Eds.), *Advanced Lectures on Machine Learning. ML 2003* (pp. 63–71). *Lecture Notes in Computer Science: Vol. 3176*. Springer. https://doi.org/10.1007/978-3-540-28650-9_4

13. Rasmussen, C.E., & Williams, C.K.I. (2005). *Gaussian Processes for Machine Learning*. The MIT Press.

14. Shen, G., & Glinka, G. (1991a). Determination of weight functions from reference stress intensity factors. *Theoretical and Applied Fracture Mechanics*, *15*(3), 237–245. https://doi.org/10.1016/0167-8442(91)90022-c

15. Shen, G., & Glinka, G. (1991b). Weight functions for a surface semi-elliptical crack in a finite thickness plate. *Theoretical and Applied Fracture Mechanics*, *15*(3), 247–255. https://doi.org/10.1016/0167-8442(91)90023-D

16. Shen, G., Plumtree, A., & Glinka, G. (1991). Weight function for the surface point of semi-elliptical surface crack in a finite thickness plate. *Engineering Fracture Mechanics*, *40*(1), 167–176. https://doi.org/10.1016/0013-7944(91)90136-O

17. Vainshtok, V.A., & Varfolomeyev, I.V. (1990). Stress intensity factor analysis for part-elliptical cracks in structures. *International Journal of Fracture*, *46*(1), 1–24. https://doi.org/10.1007/BF00034165

18. Wang, X., & Lambert, S.B. (1995a). Local weight functions for semi-elliptical surface cracks in finite thickness plates. *Theoretical & Applied Fracture Mechanics*, *23*(3), 199–208. https://doi.org/10.1016/0167-8442(95)00022-7

19. Wang, X., & Lambert, S.B. (1995b). Stress intensity factors for low aspect ratio semi-elliptical surface cracks in finite-thickness plates subjected to nonuniform stresses. *Engineering Fracture Mechanics*, *51*(4), 517–532. https://doi.org/10.1016/0013-7944(94)00311-5

20. Wawrzynek, P.A., Carter, B.J., Hwang, C.-Y., & Ingraffea, A.R. (2010). Advances in simulation of arbitrary 3D crack growth using FRANC3Dv5. *Journal of the Computational Structural Engineering Institute of Korea*, *23*(6), 607–613.

21. Xiao, X., & Yan, X. (2008). A numerical analysis for cracks emanating from a surface semi-spherical cavity in an infinite elastic body by FRANC3D. *Engineering Failure Analysis*, *15*(1–2), 188–192. https://doi.org/10.1016/j.engfailanal.2006.11.015

22. Yang, S.T., Ni, Y.L., & Li, C.Q. (2013). Weight function method to determine stress intensity factor for semi-elliptical crack with high aspect ratio in cylindrical vessels. *Engineering Fracture Mechanics*, *109*, 138–149. https://doi.org/10.1016/j.engfracmech.2013.05.014

23. Zheng, X.J., Glinka, G., & Dubey, R.N. (1996). Stress intensity factors and weight functions for a corner crack in a finite thickness plate. *Engineering Fracture Mechanics*, *54*(1), 49–61. https://doi.org/10.1016/0013-7944(95)00171-9

Manuscript received August 2, 2025; accepted for publication January 15, 2026; published online March 10, 2026.